

Modeling of J/ψ modifications in deuteron-nucleus collisions at high energiesJ. L. Nagle,^{1,*} A. D. Frawley,^{2,†} L. A. Linden Levy,^{3,‡} and M. G. Wysocki^{1,§}¹*University of Colorado at Boulder, Boulder, Colorado 80309, USA*²*Florida State University, Tallahassee, Florida 32306, USA*³*Lawrence Livermore National Laboratory, Livermore, California 94551, USA*

(Received 13 December 2010; revised manuscript received 8 April 2011; published 28 October 2011)

Understanding the detailed production and hadronization mechanisms for heavy quarkonia and their modification in a nuclear environment presents one of the major challenges in QCD. Calculations including nuclear-modified parton distribution functions (nPDFs) and the fitting of breakup cross sections (σ_{br}) as parameters have been successful at describing many features of J/ψ modifications in proton (deuteron)-nucleus collisions. In this paper, we extend these calculations to explore different geometric dependencies of the modifications and confront them with new experimental results from the PHENIX experiment. We find that no combination of nPDFs and σ_{br} , regardless of the nPDF parameter set and the assumed geometric dependence, can simultaneously describe the entire rapidity and centrality dependence of J/ψ modifications in $d + Au$ collisions at $\sqrt{s_{NN}} = 200$ GeV. We extend these calculations to incorporate initial-state parton energy loss, which results in an improved description of the experimental data. Finally, we compare the data with previously published calculations, including coherence effects, and find them unable to describe the full rapidity and centrality dependence.

DOI: [10.1103/PhysRevC.84.044911](https://doi.org/10.1103/PhysRevC.84.044911)

PACS number(s): 25.75.-q, 25.45.-z, 24.10.Jv

I. INTRODUCTION

There are numerous theoretical approaches for calculating the modification of heavy quarkonia yields in collisions of protons (deuterons) on nuclear targets. In this paper, we explore in detail whether one of these approaches, i.e., the use of nuclear-modified parton distribution functions (nPDFs) together with a fitted breakup cross section to account for collisions with nucleons, is able to describe recently published PHENIX data on J/ψ production in $d + Au$ collisions at $\sqrt{s_{NN}} = 200$ GeV [1]. The high-statistics data were measured as a function of collision geometry and over a broad range of rapidities and thus provide stringent model constraints. We also extend this model to incorporate additional effects from initial-state parton energy loss. Finally, we compare the data with two published calculations that use quite different approaches to calculate the modification in a nuclear environment: a gluon saturation model and a model where J/ψ production is determined by coherence and color-transparency effects.

In deuteron-nucleus collisions at the Relativistic Heavy Ion Collider (RHIC), the nucleus is extremely Lorentz contracted and thus the entire interaction and traversal of the nuclear target takes place on a time scale of the order of 0.1 fm/c. Thus, one expects coherence effects to play a significant role in the physics of particle production and hadronization. When studying heavy quarkonium states, one can postulate that the initial hard production of a $c\bar{c}$ pair can be factorized from the later traversal of that pair through the remainder of the nucleus. Many calculations have utilized this factorized approach in trying to understand the nuclear modification of J/ψ yields in

proton (deuteron)-nucleus reactions (for example, see [2–5]). In this factorized framework, the modification of the initial $c\bar{c}$ pair production is obtained from nPDFs. Following the initial pair production, the effect of the disassociation of charm pairs by collisions with nucleons is accounted for by a simple breakup cross section (σ_{br}). We extend this simple calculational framework in a way that allows an investigation of some of the key underlying assumptions and whether the experimental data requires additional physical effects, including coherence effects and initial-state parton energy loss.

In Sec. II, we describe each of the elements that go into the calculation of the nuclear-modification factors. In Sec. III, we present the results of calculations made with a shadowing plus σ_{br} model and compare them with recent rapidity- and centrality-dependent PHENIX data. In Sec. IV, we show that the shadowing plus σ_{br} model is incapable of describing the rapidity and centrality dependence of the data with any combination of parameters. In Sec. V, we explore whether the addition of initial-state energy loss to the shadowing plus σ_{br} calculation allows one to improve the agreement with the data. In Sec. VI, we describe the results of additional calculations using modifications from a gluon saturation model, and a coherence and color-transparency model. Finally, we summarize our results in Sec. VII.

II. CALCULATION DETAILS

In this section, we describe the inputs required for the calculation of the nuclear-modification factors (R_{pA} or R_{dA}) for various nuclear targets and centrality selections. First, the density of partons in the nucleus is modified relative to the parton distribution function (PDF) for free nucleons, resulting in a modified number of hard scatterings that create $c\bar{c}$ pairs from $g + g$, $q + g$, and $q + \bar{q}$ interactions. This effect is included in the calculations presented here by using the

*jamie.nagle@colorado.edu

†afrawley@fsu.edu

‡lindenle@llnl.gov

§matthew.wysocki@colorado.edu

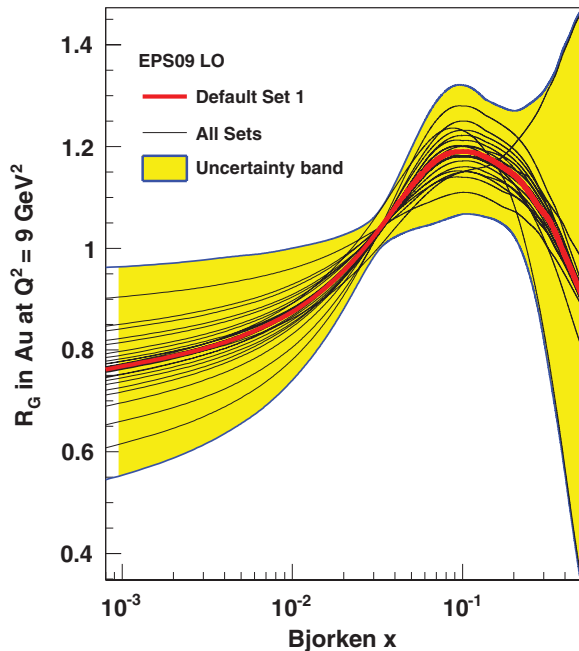


FIG. 1. (Color online) The gluon nuclear modification R_G for the Au nucleus at the scale $Q^2 = 9 \text{ GeV}^2$ is shown for the EPS09 central value (labeled set 1) and for all 30 error sets. The shaded (yellow) area is the overall uncertainty band calculated from the error sets, representing a 90% C.L. uncertainty.

state-of-the-art EPS09 nPDF parameter set, with uncertainties represented by 31 different Hessian basis parametrizations as detailed in [6]. Because J/ψ production at high energies is dominated by interactions between gluons, we will consider only $g + g$ interactions in the calculations presented in this paper. Figure 1 shows the EPS09 gluon modification R_G at $Q^2 = 9 \text{ GeV}^2$, which is the appropriate scale for production of the J/ψ . It can be seen that the nPDFs are not well constrained by experimental data, particularly the low- x gluon distributions, which dominate the J/ψ production probability at forward rapidity at RHIC energies.

The second main effect is that after the $c\bar{c}$ pair is created in the initial state (this is frequently referred to as the J/ψ precursor, since the hadronic state is expected to take of the order of $0.3 \text{ fm}/c$ to form), the pair may break up or be decorrelated while traversing the remaining portion of the nucleus. This second effect is often included by assuming a constant cross section σ_{br} for the breakup of the pair. We note that this effect is also sometimes termed absorption, though this nomenclature can be misleading, since the charm pair still exists but is no longer able to form a final-state J/ψ meson. Currently there is no fundamental description of the hadronization process for the J/ψ that agrees with all the available experimental data [7,8]. The lack of such a theory for the dynamics of hadronization means one has no *ab initio* calculation of this precursor-nucleon cross section and its dependence on the relative velocity between the pair and the target nucleons. In most works, the value of σ_{br} is assumed to be independent of the J/ψ rapidity for a given $\sqrt{s_{NN}}$, and is determined from fits to the experimental data [9].

A. Nuclear geometry

In order to account for the geometric dependence of the two above-mentioned effects, we employ a Monte Carlo Glauber model [10]. The nucleons are randomly given spatial distributions within the deuteron based on the Hulthen wave function, and within the gold nucleus based on a Woods-Saxon distribution with parameters $R = 6.38 \text{ fm}$ and $a = 0.54 \text{ fm}$ [3]. Individual $d + \text{Au}$ collisions at $\sqrt{s_{NN}} = 200 \text{ GeV}$ are simulated by randomly selecting an event impact parameter (b) and determining if any pair of nucleons collide using an inelastic cross section of $\sigma = 42 \text{ mb}$. One example event is shown in Fig. 2, where the open circles are the positions of the gold-nucleus nucleons in the transverse plane, the darker (red) filled circles are the positions of the two nucleons from the deuteron, and the lighter (green) filled circles are the positions of the gold-nucleus nucleons which suffered a binary collision. Each binary collision between a deuteron nucleon and a gold nucleon has a certain probability to produce a $c\bar{c}$ pair. This probability is modified from proton-proton collisions according to the aforementioned nPDFs.

The EPS09 nPDF parametrization, as well as other nPDF parameterizations, are predominantly determined from deep inelastic-scattering experiments and minimum-bias $p + A$ reactions producing Drell-Yan pairs [6]. In such experiments, there is no measure of the impact parameter or transverse distance within the nucleus for the interaction and therefore the geometric dependence of the nPDF modification is not constrained.

The partons inside the nucleons at low x have wave functions that are longer in the longitudinal direction than the size of the Lorentz contracted nucleus. Thus the nPDF

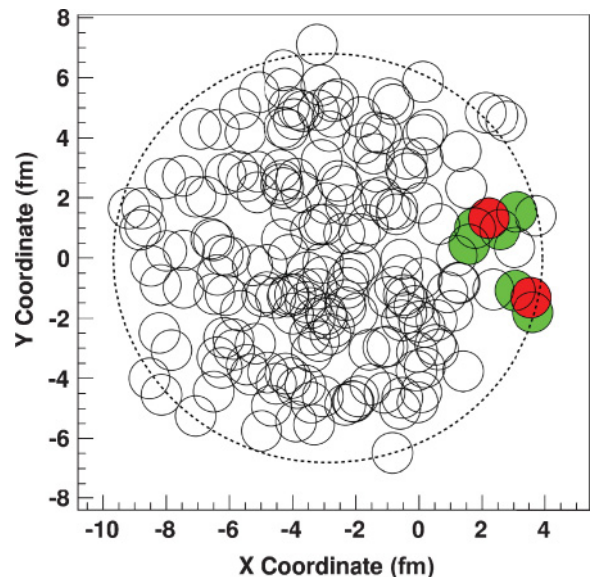


FIG. 2. (Color online) Monte Carlo Glauber event display in the transverse (x - y) plane. Open circles are the positions of the gold-nucleus nucleons. Dark (red) filled circles are the positions of the two nucleons from the deuteron. Light (green) filled circles are the positions of the gold-nucleus nucleons which suffer at least one binary collision. The large dashed circle represents the gold-nucleus radius used in the Woods-Saxon parametrization.

modification depends on the density of overlapping nucleons, as shown in the transverse plane in Fig. 2. However, there is no such Lorentz contraction in the transverse direction, and the parton wave-function extent in this plane is of the order of 1 fm. Therefore, the largest nuclear effect would be expected where the density, and thus the longitudinal overlap, is largest, which is near the center of the nucleus, and should decrease as one moves out toward the periphery.

In Ref. [11], the nPDF modification is postulated to be linearly proportional to the density-weighted longitudinal thickness of the nucleus at the transverse position of the binary collision,

$$M(r_T) = 1.0 - a\Lambda(r_T), \quad (1)$$

where $\Lambda(r_T) = \frac{1}{\rho_0} \int dz \rho(z, r_T)$ is the density-weighted longitudinal thickness and ρ_0 is the density at the center of the nucleus. In Fig. 2, each gold nucleus is a transverse distance r_T from the center of the gold nucleus, and the corresponding average local thickness $\Lambda(r_T)$ is determined from the Woods-Saxon parametrization.

Figure 2 shows that there are significant fluctuations in the thickness $\Lambda(r_T)$ due to the randomly selected spatial locations of the nucleons in the gold nucleus at the time of the collision. In fact, the inclusion of such fluctuations has proven crucial for modeling the initial conditions in heavy-ion reactions (see, for example, [12–16]). In order to incorporate these fluctuations, we calculate the number of target nucleons around the struck target nucleon within a transverse radius, $R_{\text{tube}} = 2 \times R_{\text{nucleon}}$, where R_{nucleon} is taken to be the charge radius of the proton, which is 0.87 fm [17]. The average number of nucleons within this cylinder N_{tube} is $\pi R_{\text{tube}}^2 \rho_0 \times \Lambda(r_T)$, and the proportionality constant can be absorbed into the parameter a in Eq. (1). The exact choice of R_{tube} is somewhat arbitrary, but reasonable changes of its value do not significantly change the results shown in this paper.

Figure 3 shows the two-dimensional (2D) correlation between N_{tube} and r_T that results from this Monte Carlo (MC) calculation. The mean value of N_{tube} as a function of r_T is shown as white points. For collisions in the middle of the nucleus, the average value of N_{tube} is ≈ 20 and the rms is ≈ 5 . An analytic calculation of the average $\Lambda(r_T)$ from the Woods-Saxon parametrization times $\pi R_{\text{tube}}^2 \rho_0$ yields the solid red curve. The analytic calculation differs from the mean of the MC calculation because the MC calculation effectively averages the density over the tube radius R_{tube} . If we smear the analytic calculation around r_T by R_{tube} , we obtain the red dashed curve, which is in much better agreement with the average of the MC results.

In our calculations, we take these fluctuations into account by utilizing N_{tube} instead of the average value of $\Lambda(r_T)$:

$$M(r_T) = 1.0 - aN_{\text{tube}}(r_T). \quad (2)$$

There is a direct relationship between the parameter a and $\langle M \rangle$, which is the modification averaged over all nuclear geometries, and this is equivalent to the observable nuclear-modification factor averaged over the entire collision centrality range. If the centrality of an event varies between 0% (most central collision) and 100% (least central collision), the observable modification averaged over all centrality is represented by

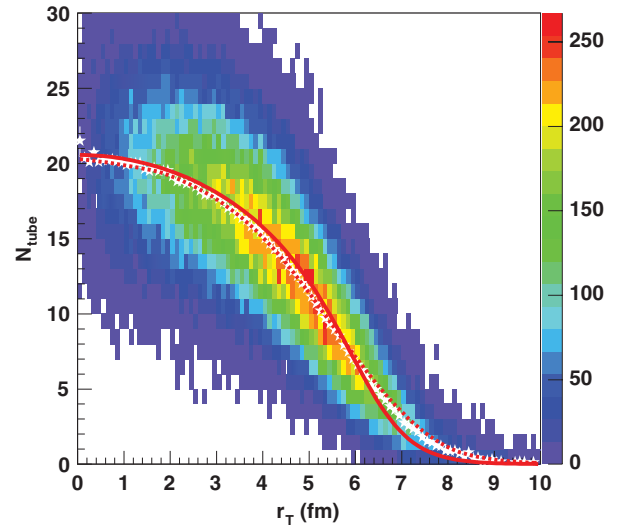


FIG. 3. (Color online) The Monte Carlo Glauber results for the N_{tube} as a function of r_T . The mean values of N_{tube} as a function of r_T are shown as white points. The analytic calculation of the average value of $\Lambda(r_T)$ from the Woods-Saxon parametrization, rescaled to the N_{tube} value, is shown as the solid (red) curve. Smearing the analytic calculation around r_T by the tube radius R_{tube} yields the dashed (red) curve.

$R_{d\text{Au}}(0-100\%)$. The relationship between a and $R_{d\text{Au}}(0-100\%)$ is determined by averaging M over the r_T distribution for unbiased collisions, as determined from the Glauber Monte Carlo (shown in Fig. 3 of the PHENIX publication [1]). The results are shown as the solid curve in Fig. 4. We also consider two other geometric dependencies for the nPDF:

$$M(r_T) = \exp[-aN_{\text{tube}}(r_T)], \quad (3)$$

$$M(r_T) = 1.0 - a[N_{\text{tube}}(r_T)]^2, \quad (4)$$

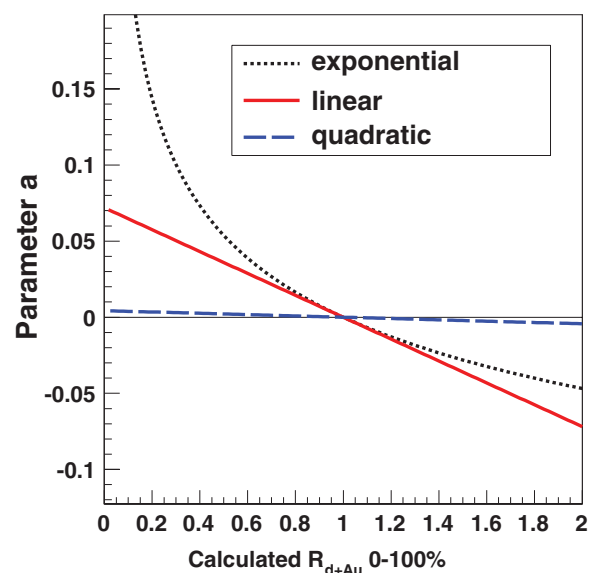


FIG. 4. (Color online) The parameter a as a function of $R_{d\text{Au}}(0-100\%)$. The curves correspond to linear, exponential, and quadratic geometric dependence.

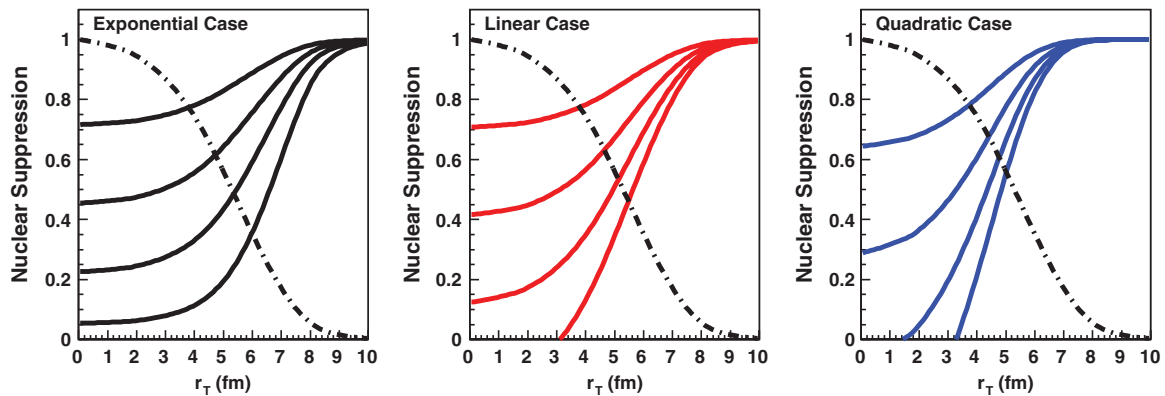


FIG. 5. (Color online) The modification dependencies $M(r_T)$ for the three geometry cases (exponential, linear, and quadratic) assuming four different average $R_{d\text{Au}}(0-100\%)$ values: 0.8, 0.6, 0.4, 0.2 (from the top to bottom curves in each case). The dot-dashed black line is N_{tube} as a function of r_T , normalized to unity at $r_T = 0$, which is shown for reference.

which are referred to as exponential and quadratic, respectively. Figure 4 shows the dependence of the parameter a on $R_{d\text{Au}}(0-100\%)$ as the dotted (dashed) curve for the exponential (quadratic) case.

We examine the modification $M(r_T)$ for each of these cases. Figure 5 (left panel) shows $M(r_T)$ for the exponential case. The four curves correspond to geometry-averaged modifications of $\langle M \rangle = 0.8, 0.6, 0.4, 0.2$, from the top to bottom curves. The dot-dashed black line is the shape of the mean of the N_{tube} distribution versus r_T , normalized to unity at $r_T = 0$, which is shown for reference. The middle (right) panel shows the same results for the linear (quadratic) case. As a consequence of the linear and quadratic functional forms, $M(r_T)$ has negative values for small r_T when the geometry-averaged modification is less than 0.4 (0.6) for the linear (quadratic) cases. This unphysical result can be removed by forcing the modification to be positive definite, and recalculating the corresponding a parameter. In the analysis presented in this paper, the modification values from the nPDF do not typically reach these low values, and thus we did not have to recalculate the results. However, careful attention to this problem will be crucial for cases with larger modifications (for example, more forward rapidity J/ψ measurements or very-low- x measurements at the Large Hadron Collider in $p + A$ and $A + A$).

B. Parton kinematics

There are two final ingredients needed to map the nPDF modifications onto the final-state J/ψ suppression. These are the distributions of Bjorken x_2 and Q^2 for the parton-parton processes that contribute to J/ψ production, and the mixture of $g + g$, $g + q$, and $q + \bar{q}$ processes. The simplest relationship between the J/ψ and partonic kinematics arises under the assumption that the production is a $2 \rightarrow 1$ process, for example, $g + g \rightarrow J/\psi$. By invoking conservation of energy and momentum, the production of a J/ψ with $p_T = 0$ GeV/c results in the following relationship between J/ψ rapidity (y) and the parton momentum fraction (x_2):

$$x_2 = \frac{M_{J/\psi}}{\sqrt{s_{NN}}} e^{-y}. \quad (5)$$

This $2 \rightarrow 1$ process is actually forbidden by angular momentum conservation, but may approximate the correct kinematics at low p_T , or in a color-evaporation picture where soft gluon emission does not significantly modify the exact correlation between x_2 and y . It has been pointed out that with a more detailed understanding of the subprocesses that contribute to J/ψ production, one can utilize a more exact map of x_2 and Q^2 to the final J/ψ as a function of rapidity and p_T [18–20]. The authors utilize the following relation between x_1 and x_2 that requires a full modeling of the cross-section dependencies:

$$x_2 = \frac{x_1 \sqrt{p_T^2 + M^2} \sqrt{s_{NN}} e^{-y} - M^2}{\sqrt{s_{NN}} (\sqrt{s_{NN}} x_1 - \sqrt{p_T^2 + M^2} e^y)}. \quad (6)$$

This relation is exact for a $2 \rightarrow 2$ process where one outgoing particle is an on-shell J/ψ and the other particle is massless.

Figure 6 (upper panel) shows the correlation between Bjorken x_2 and the J/ψ rapidity in the $2 \rightarrow 1$ case. This is compared with a scatterplot showing calculation results from PYTHIA 6.416 [21] with the nonrelativistic QCD (NRQCD) setting for J/ψ production. As expected, the x_2 values for a given J/ψ rapidity are shifted to larger values. Since the J/ψ $\langle p_T \rangle \approx 2.2$ GeV/c, there must be one or more balancing particles, which requires larger available energy. Additionally, the emission of a balancing gluon or gluons smears the rapidity of the J/ψ relative to the $2 \rightarrow 1$ calculation. Also shown are the $\langle x_2 \rangle$ values as a function of rapidity for the PYTHIA $g + g$ color singlet channel, $g + g$ color octet channel, and the $q + g$ color octet channel. The mean x_2 value can be misleading since it may have a large influence from a small fraction of high- x events. Thus, in the lower panel, we show the $\log_{10}(x_2)$ distribution for the J/ψ rapidity range $2.0 < y < 2.4$ for the three different contributions. The majority of processes for this rapidity involve $x_2 \approx 0.002$, but with a more significant high- x tail in the octet cases. Note that the underlying PYTHIA production does not obey the $2 \rightarrow 2$ kinematics of Eq. (6), since there is initial-state k_T and many of the octet production channels involve more than two final-state particles.

We now incorporate all of the following items: (1) Monte Carlo Glauber, (2) deuteron and gold nuclear geometries,

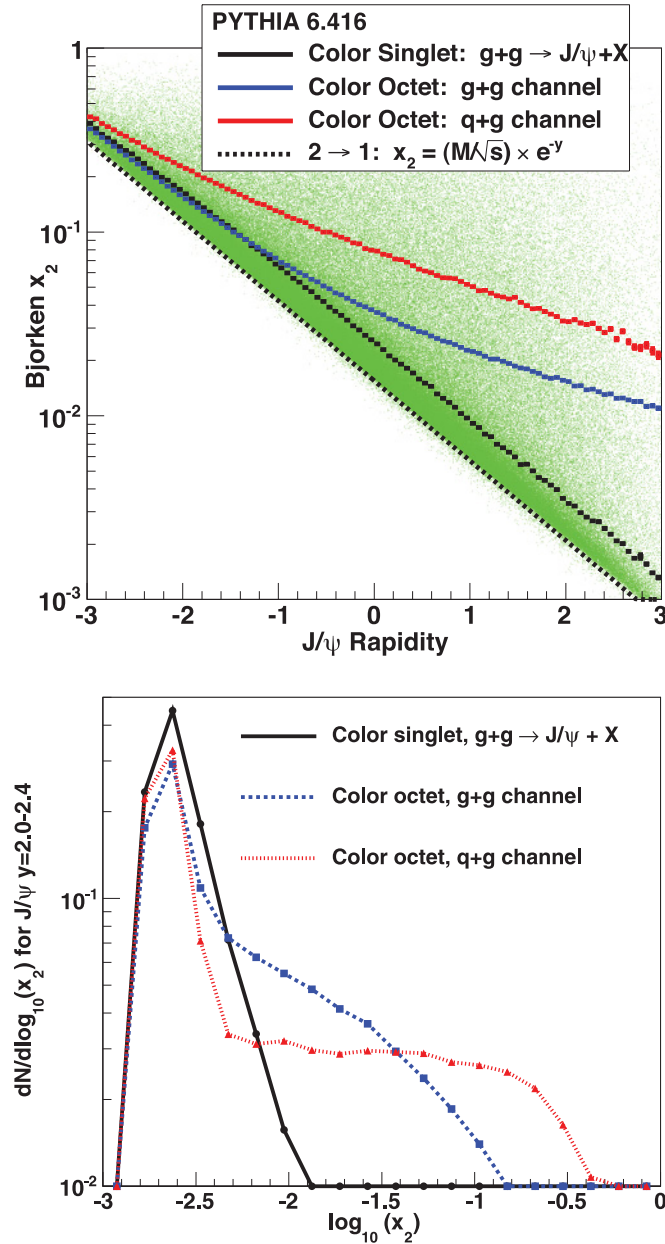


FIG. 6. (Color online) Upper panel: The kinematic correlations between the J/ψ rapidity and Bjorken x_2 for the $2 \rightarrow 1$ process compared with a scatterplot showing calculations from PYTHIA 6.416 with the NRQCD setting for J/ψ production. The $\langle x_2 \rangle$ values are shown for three different production mechanisms within PYTHIA 6.416. Lower panel: The x_2 distributions for J/ψ produced with rapidity $2.0 < y < 2.4$ are shown for the three different PYTHIA production mechanisms.

(3) EPS09 nPDF parameter set, (4) geometric-dependence assumption for nPDF (linear, quadratic, exponential), and (5) kinematic mapping ($g, q, \bar{q}, x_2, Q^2 \rightarrow J/\psi$ y, p_T). We then add the second factorized part of the calculation by using the cross section σ_{br} to test if the $c\bar{c}$ pair is broken up by collisions with those nucleons having $z_{\text{nucleon}} > z_{\text{binary}}$ that reside in a tube of radius R_{tube} around the production point. Note that although the calculations are factorized, the results

are autocorrelated by the geometry. For example, a binary collision occurring near $r_T = 0$ has a larger nPDF modification and also a larger probability of breakup. These autocorrelations are important to account for, and have been previously explored in terms of k_T kicks broadening the p_T distribution [22,23].

Two additional benefits of this Monte Carlo Glauber approach with full fluctuations are that we can model the exact PHENIX experimental $d + \text{Au}$ centrality selection event by event, and that we never project onto an averaged quantity (e.g., the average impact parameter for each centrality class) and then calculate the modification for that average quantity.

III. CALCULATION RESULTS

Gathering all of these pieces together, we show an example calculation in Fig. 7 of the J/ψ nuclear modification as a function of rapidity for the centrality integrated case, $R_{d\text{Au}}(0-100\%)$. In this example, we utilize the $2 \rightarrow 1$ exact process mapping and the linear geometric dependence of the nPDFs. We show the default EPS09 result with $\sigma_{br} = 4$ mb, all 30 other variations for EPS09 with $\sigma_{br} = 4$ mb, and a calculation assuming no nPDF modification with $\sigma_{br} = 4$ mb. The PHENIX experiment has recently reported high-statistics nuclear-modification factors from J/ψ $d + \text{Au}$ measurements at $\sqrt{s_{NN}} = 200$ GeV as a function of rapidity [1]. The centrality unbiased data are shown in Fig. 7. The calculation and experimental data agree within systematic uncertainties.

We emphasize that this calculation utilized the $2 \rightarrow 1$ kinematics. We have performed the same calculation using

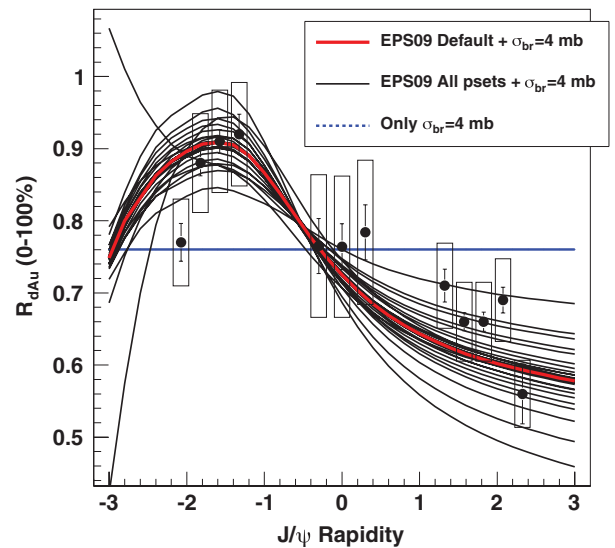


FIG. 7. (Color online) The J/ψ nuclear-modification factor $R_{d\text{Au}}$ for 0–100% interaction centrality as a function of rapidity. The calculations include the EPS09 nPDFs with the linear geometric dependence and $2 \rightarrow 1$ kinematics. All 31 EPS09 nPDF variations are shown. These should not be interpreted as a one-standard-deviation uncertainty band. The PHENIX experimental data are shown as points. The vertical lines are the point-to-point uncorrelated uncertainties and the boxes are the point-to-point correlated systematic uncertainties. Not shown is the additional $\pm 7.8\%$ global scale uncertainty.

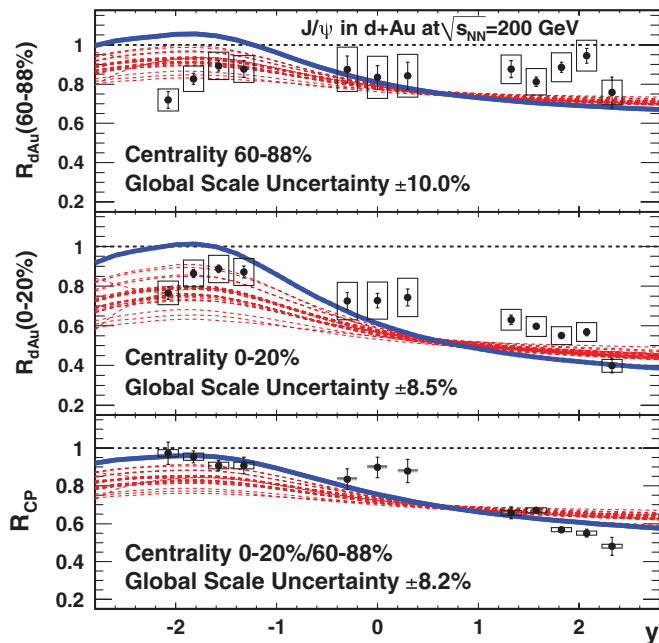


FIG. 8. (Color online) Comparison of PHENIX data with calculations (dashed curves) using the 31 EPS09 parameter sets with linear nuclear-thickness dependence. Each EPS09 parameter set is shown for its own best fit σ_{br} value to the R_{CP} pattern. The solid (blue) curve was obtained with EPS09 set 17 and $\sigma_{br} = 3.2$ mb. It provides the best overall fit to the R_{CP} data, despite failing to reproduce the R_{dAu} patterns.

the various PYTHIA kinematics and find only a very modest change in the rapidity dependence, which in the calculation comes entirely from the nPDF dependence on x_2 and Q^2 . Utilizing the PYTHIA kinematics leads to a slight blurring of this relation and a general shift to larger x_2 values, as expected from Fig. 6. This in turn leads to a flattening of the calculated R_{dAu} versus rapidity curve, and to slightly poorer agreement with the data. However, the uncertainties in the nPDFs do not allow any conclusion to be drawn about the underlying production process.

Figure 8 shows the PHENIX experimental nuclear-modification factors for peripheral events, $R_{dAu}(60-88\%)$ (top panel), for central events, $R_{dAu}(0-20\%)$ (middle panel), and the ratio between them R_{CP} 0–20%/60–88% (lower panel). Note that the significant systematic uncertainties in the rapidity dependence of the modification, shown as boxes in the figure, and referred to by PHENIX as type-B systematics, largely cancel in the R_{CP} ratio.

We utilize the r_T distributions for each centrality class shown in Fig. 3 of the PHENIX publication [1] to compute the expected modification in each centrality. There are many different statistical fits one can perform between the experimental data and our theoretical calculations. In this case, we perform a modified- χ^2 ($\tilde{\chi}^2$) fit to just the R_{CP} data (which provides by far the best constraint on the rapidity dependence). The $\tilde{\chi}^2$ -fit method, which accounts for both statistical and systematic uncertainties, is detailed in Ref. [24].

We consider the linear, quadratic, and exponential geometric dependencies for the nPDFs. Figure 8 shows the results for

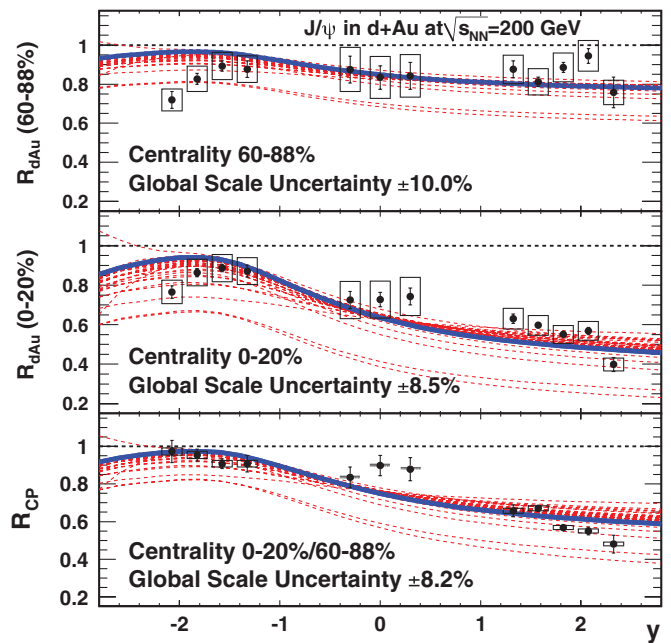


FIG. 9. (Color online) Comparison of PHENIX data with calculations (dashed curves) using the 31 EPS09 parameter sets with quadratic nuclear-thickness dependence. Each EPS09 parameter set is shown for its own best-fit σ_{br} value to the R_{CP} pattern. The solid (blue) curve was obtained with EPS09 set 30 and $\sigma_{br} = 3.4$ mb. It provides the best overall fit to the R_{CP} data, despite failing to reproduce the R_{dAu} patterns.

the linear geometric dependence. Each dashed curve represents one of the 31 EPS09 nPDF parameter sets and the best fit σ_{br} value for that parameter set (i.e., minimum $\tilde{\chi}^2$) to the R_{CP} data. The corresponding result is also shown for R_{dAu} peripheral and central in the upper and middle panels, respectively. The solid curve represents the best fit of all combinations of EPS09 parameter sets and σ_{br} values—corresponding to EPS09 nPDF parameter set 17 and a $\sigma_{br} = 3.2$ mb. However, even this best fit has a $\tilde{\chi}^2 = 41.5$, which corresponds to an extremely poor fit (i.e., probability less than 10^{-4}). The result with the geometric nPDF exponential case is similar with the best fit from EPS09 nPDF parameter set 17 and $\sigma_{br} = 4.2$ mb and a poor $\tilde{\chi}^2 = 50.6$.

The results for the quadratic geometric dependence are shown in Fig. 9. The best fit now corresponds to EPS09 parameter set 30 and $\sigma_{br} = 3.4$ mb. Again, even this best fit has a $\tilde{\chi}^2 = 46.3$, which corresponds to an extremely poor fit. One notable feature that is counterintuitive is that for some EPS09 nPDF parameter sets, the best fit shown by the dashed curve is far below the R_{CP} data points. Because the rapidity shape is so poorly matched, it is possible that a better fit is obtained under the assumption that the global scale uncertainty of 8.2% has a three-standard-deviation fluctuation low.

IV. NEW GEOMETRIC CONSTRAINTS

In Ref. [1], the PHENIX collaboration presented a new way of constraining the geometric dependence of the combined nuclear effects. By plotting R_{CP} (0–20%/60–88%) versus

the geometry-averaged nuclear modification $R_{dAu}(0-100\%)$, there are constrained parametric dependencies for the linear, exponential, and quadratic cases. In Ref. [1], the analytic parametrization for $M(r_T)$ as a function of the average $\Lambda(r_T)$ was used to compare the nuclear modification in all centralities for a given value of parameter a . For a particular geometric dependence, varying the values of a results in a locus of points for the constrained relationship between R_{dAu} and R_{CP} . Figure 10 shows, as dotted, solid, and dashed black lines, the result of that analytic calculation for the exponential, linear, and quadratic cases, respectively. To be clear, these curves are calculated purely from the Monte Carlo Glauber geometry, the average density-weighted nuclear thickness $\Lambda(r_T)$, and the simple geometric-dependence equation (i.e., no specific model of nPDFs, σ_{br} , etc.). Also shown are the PHENIX experimental data with the lines as point-to-point uncorrelated uncertainties and the ellipses as one-standard-deviation contours from the combined systematic uncertainties. As stated in Ref. [1], this demonstrates that the forward rapidity J/ψ data cannot be reconciled with an exponential or linear geometric dependence for the nuclear modification.

We pursue this test one step further by plotting the results from our calculations using the EPS09 nPDFs and σ_{br} model. Figure 10 shows all EPS09 nPDF parameter sets using the exponential geometric dependence, a range of

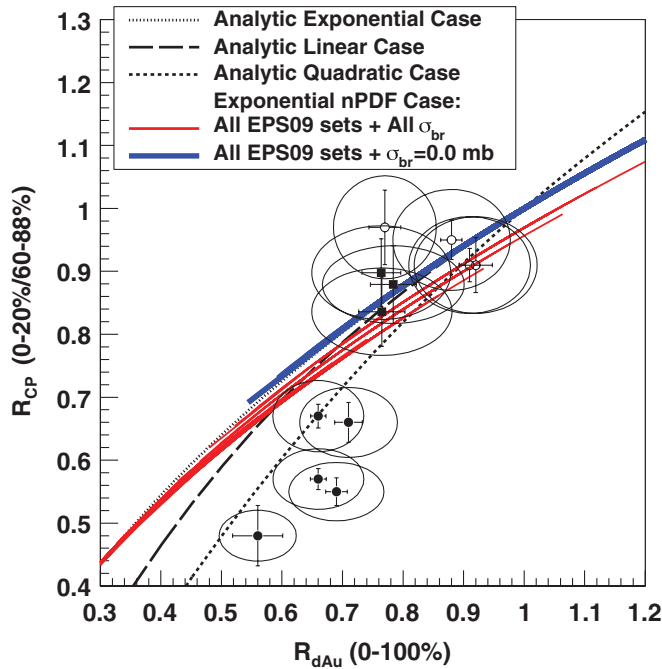


FIG. 10. (Color online) The points are the PHENIX J/ψ R_{CP} plotted vs R_{dAu} . The ellipses are the one-standard-deviation contours for the systematic uncertainties. The open circles, closed squares, and closed circles are from backward, mid, and forward rapidity, respectively. Analytic calculations are shown that assume a purely exponential, linear, or quadratic geometric dependence for the nuclear modification [1]. The full calculation with an exponential thickness dependence for the shadowing is shown for all EPS09 nPDF parameter sets with $\sigma_{br} = 0$, and also for all EPS09 nPDF parameter sets with all σ_{br} values.

values of σ_{br} (from 0–18 mb, in 2 mb steps) and the full range of rapidity values. The subset corresponding to $\sigma_{br} = 0$ is shown separately, as the thick line. As expected, since the nPDF dependence is exponential, the $\sigma_{br} = 0$ lines fall almost perfectly on the analytic pure exponential case. With a nonzero σ_{br} contribution, which also has an exponential geometric dependence, we expected that everything would collapse onto the same line. However, with two competing effects, $R_{dAu}(0-100\%) = 1$ does not always equate with the trivial case of no modification, but can also occur if the two effects average to 1. In the latter case, R_{CP} need not be 1. Specifically in our case, in the backward rapidity region, the nPDF leads to an enhancement (antishadowing) and a nonzero σ_{br} to a suppression. This competition can lead to the case where $R_{dAu}(0-100\%) = 1$, while the $R_{CP} \neq 1$ (i.e., modest enhancement in peripheral events due to the nPDF effect and modest suppression in central events due to the σ_{br} effect). This effect leads to the slight splitting of the $\sigma_{br} > 0$ lines for values near $R_{dAu} = 1$.

Figure 11 shows the same quantities for the case of linear geometric dependence of the nPDF in our calculation. Again, the case with $\sigma_{br} = 0$ leaves only the purely linear nPDF and thus these lines collapse onto the analytic linear case. The curves for all $\sigma_{br} > 0$ cases result in a geometric dependence that is part linear and part exponential. Thus, one sees that for larger suppressions (due to larger σ_{br} values), the curves move

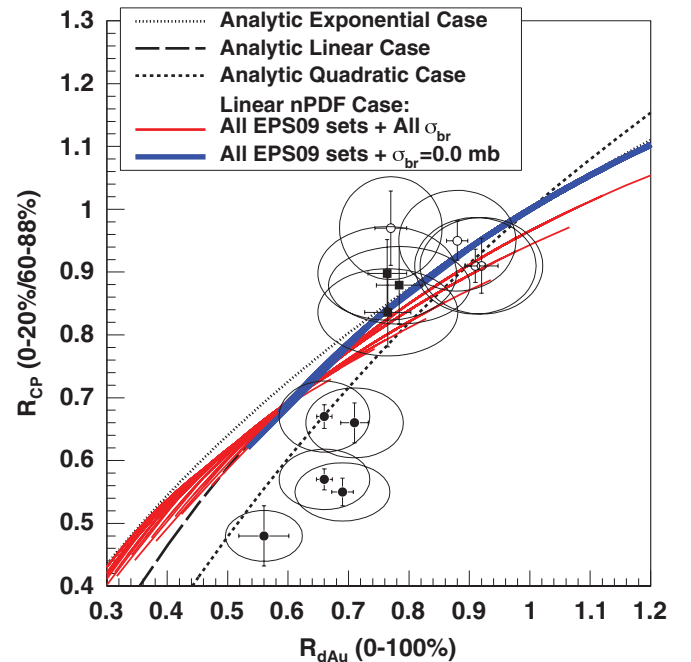


FIG. 11. (Color online) The points are the PHENIX J/ψ R_{CP} vs R_{dAu} . The ellipses are the one-standard-deviation contours for the systematic uncertainties. The open circles, closed squares, and closed circles are from backward, mid, and forward rapidity, respectively. Analytic calculations are shown that assume a purely exponential, linear, or quadratic geometric dependence for the nuclear modification [1]. The full calculation with a linear thickness dependence for the shadowing is shown for all EPS09 nPDF parameter sets with $\sigma_{br} = 0$, and for all EPS09 nPDF parameter sets with all σ_{br} values.

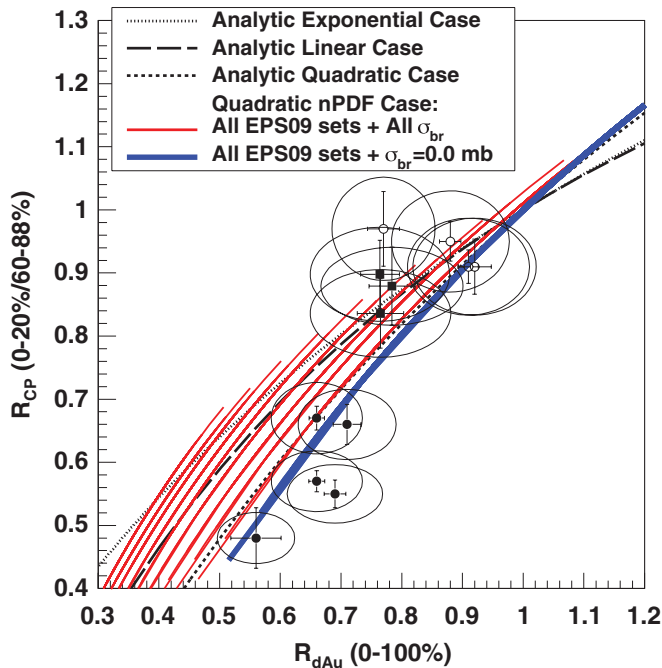


FIG. 12. (Color online) The points are the PHENIX J/ψ R_{CP} vs R_{dAu} . The ellipses are the one-standard-deviation contours for the systematic uncertainties. The open circles, closed squares, and closed circles are from backward, mid, and forward rapidity, respectively. Analytic calculations are shown that assume a purely exponential, linear, or quadratic geometric dependence for the nuclear modification [1]. The full calculation with a quadratic thickness dependence for the shadowing is shown for all EPS09 nPDF parameter sets with $\sigma_{br} = 0$, and for all EPS09 nPDF parameter sets with all σ_{br} values.

between the analytic linear case to the analytic exponential curve. One again sees some cases where $R_{dAu}(0-100\%) = 1$ while R_{CP} is not equal to one, for the same reason as described above.

Lastly, Fig. 12 shows the results for the quadratic case. In this case, the $\sigma_{br} = 0$ lines are close to the analytic quadratic case, but not a perfect match. This disagreement results from the inclusion of fluctuations in the thickness in our full calculation. As one increases the value of σ_{br} in 2 mb increments, the lines move to the left as the exponential geometric dependence from σ_{br} dominates over the quadratic nPDF effect.

This full suite of curves reveals that even attempting to fit just the forward rapidity data with a larger and larger σ_{br} will not successfully capture the full centrality dependence (even using the quadratic nPDF contribution).

The results of fitting R_{CP} shown in Figs. 8 and 9 demonstrated that no variation in the model (e.g., EPS09 nPDF parameter sets, nPDF geometric dependence, single σ_{br} values, etc.) can be reconciled with the full rapidity and centrality dependence of the experimental data. It is possible that σ_{br} may have a rapidity dependence due to the different relative velocity of the $c\bar{c}$ pair with respect to the target nucleons. A naïve expectation is that a shorter time spent in the nucleus should result in a smaller σ_{br} due to a smaller growth in the physical size of the $c\bar{c}$ pair toward that of the final state J/ψ . However,

in order to attempt to describe the data with a rapidity-dependent σ_{br} , the cross section would need to be much larger at larger rapidity (as shown in Ref. [25] in section 5.2).

V. INITIAL-STATE ENERGY LOSS

Energy loss in the nucleus of the incoming parton upstream of the hard process is another effect that may impact J/ψ yields in deuteron-nucleus collisions. Forward rapidity J/ψ are produced from a high- x_1 parton (from the deuteron) and a low- x_2 parton (from the gold nucleus). If the high- x_1 parton from the deuteron loses energy before the hard scattering, the result will be a smaller J/ψ production probability and a shift backward in rapidity for any produced particles (including the J/ψ). This framework has been used to reproduce lower-energy Drell-Yan data in $p + A$ collisions (see, for example, [26,27]). However, the same data have also been interpreted in terms of nuclear shadowing models without initial-state energy loss.

More recently, in Ref. [28], a calculation is presented of initial-state parton energy loss and its impact on Drell-Yan production with predictions for measurements in $p + A$ collisions. In the case of initial-state radiative energy loss, they predict that $\Delta E/E \propto L$, where L is the path through the nucleus prior to the hard scattering. Drell-Yan data from experiment E906 at Fermilab will directly address this prediction [29].

We have implemented this energy-loss mechanism in our calculation (in addition to the nPDF and σ_{br} contributions). Within the Monte Carlo Glauber, we also calculate $N_{\text{tube}}[\text{before}]$, which is the number of gold-nucleus nucleons in the tube that have a z location prior to the z position of the binary collision of interest. We posit that the initial-state energy loss is proportional to $N_{\text{tube}}[\text{before}]$, which is the same as being proportional to the path L , with the inclusion of local fluctuations. For this calculation, we have utilized the PYTHIA production $g + g \rightarrow J/\psi + X$ kinematics. For each binary-collision location, we randomly select a PYTHIA x_1, x_2 combination and the mean J/ψ rapidity for those kinematics. We then calculate the expected x_1 shift due to the energy loss corresponding to the particular $N_{\text{tube}}[\text{before}]$ value. From this information, we calculate the decrease in the probability for these partons to produce a $c\bar{c}$ pair and the new (lower) average final-state J/ψ rapidity with the modified parton kinematics. We have varied the proportionality constant for the initial-state energy loss in the $N_{\text{tube}}[\text{before}]$ dependence.

Figure 13 (left panel) shows results including only initial-state parton energy loss (i.e., no nPDF modification and $\sigma_{br} = 0$), with a linear path-length dependence. One observes a larger suppression at forward rapidity, and in fact a modest enhancement at backward rapidity. Figure 13 (right panel) shows the results when a quadratic path-length dependence is assumed for the energy loss (i.e., $\Delta E/E \propto L^2$). In this case, for large values of the proportionality constant, there is large suppression at all rapidities. For either the L or L^2 dependence, one cannot achieve good agreement with the experimental data with initial-state parton energy loss alone.

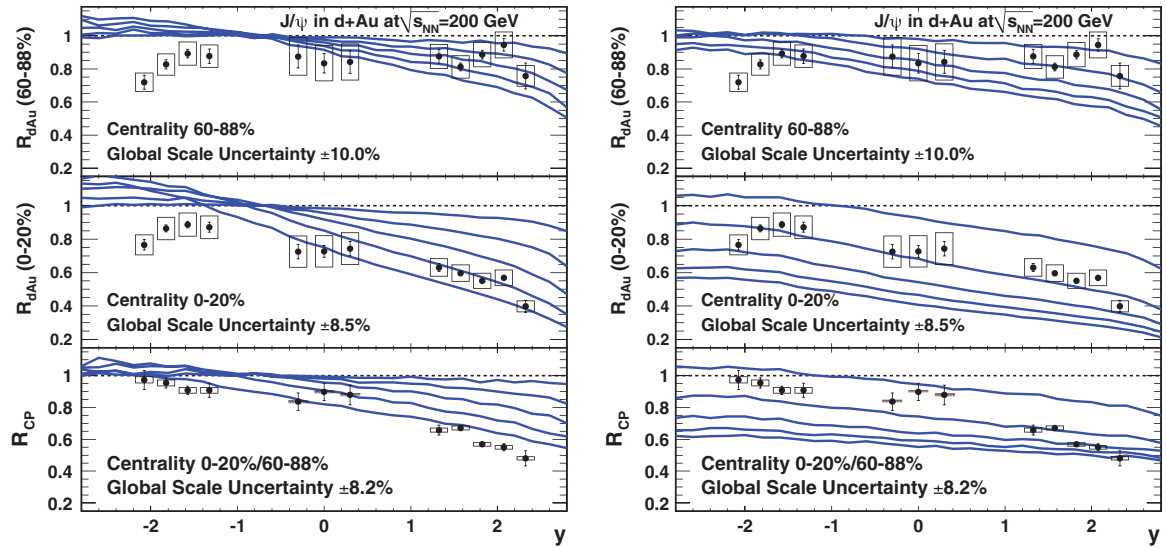


FIG. 13. (Color online) Left panel: Calculation including initial-state parton energy loss only, and with $\Delta E/E \propto L$, where L is taken to be $N_{\text{tube}}[\text{before}]$ to include fluctuations. The curves correspond to coefficients of 0.01, 0.03, 0.05, 0.07, and 0.09/fm (from upper to lower, respectively, at large rapidity). Right panel: Calculation including initial-state parton energy loss only, and with $\Delta E/E \propto L^2$, where L^2 is taken to be $N_{\text{tube}}^2[\text{before}]$ to include fluctuations. The curves correspond to coefficients of 0.005, 0.015, 0.025, 0.035, and 0.045/fm² (from upper to lower, respectively, at large rapidity).

We then include all three nuclear effects (nPDF modification, σ_{br} , and initial-state parton energy loss), and vary the EPS09 nPDF parameter set and fit for the best σ_{br} and energy-loss coefficient. Figure 14 (left panel) shows the results of finding the best $\tilde{\chi}^2$ for fits to the R_{CP} with all EPS09 parameter sets, assuming a linear path-length dependence for the initial-state energy loss. The solid curve represents the best fit of all of the EPS09 parametrizations after optimizing σ_{br} and the initial-state energy-loss coefficient. The best fit gives a reasonable description of the R_{CP} . It corresponds to EPS09 parameter

set 23, $\sigma_{br} = 3$ mb, and $\Delta E/E \approx 0.05/\text{fm} \times L$ (converting the average $N_{\text{tube}}[\text{before}]$ to a length through normal nuclear-matter density). The $\tilde{\chi}^2$ of 20.2 is a better fit than without the initial-state energy loss, but still gives a probability of less than 5%. Although the fit to the R_{CP} is reasonable, there is no global agreement with the data for R_{dAu} in peripheral or central events.

Figure 14 (right panel) shows the same quantities under the assumption that the initial-state energy loss is quadratic in the path or $N_{\text{tube}}[\text{before}]$. In this case, the best fit to R_{CP} has

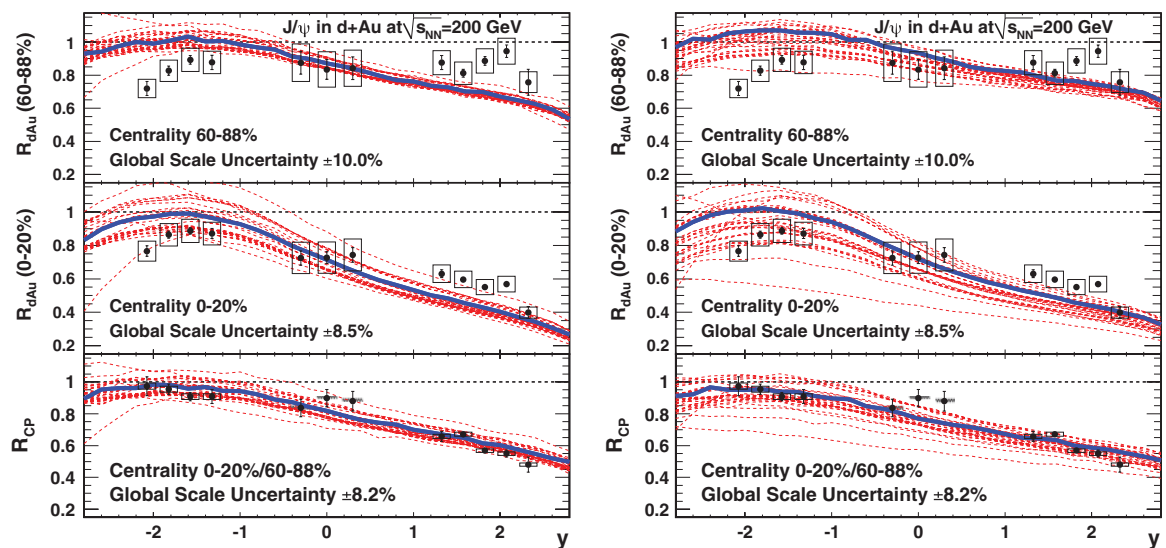


FIG. 14. (Color online) Left panel: Best fit to the R_{CP} data including initial-state parton energy loss, assuming the loss is proportional to $N_{\text{tube}}[\text{before}]$. The solid (blue) curve shows the best fit of all of the EPS09 parameter sets. Right panel: Best fit to the R_{CP} data including initial-state parton energy loss, assuming the loss is proportional to $N_{\text{tube}}^2[\text{before}]$. The solid (blue) curve shows the best fit of all of the EPS09 parameter sets.

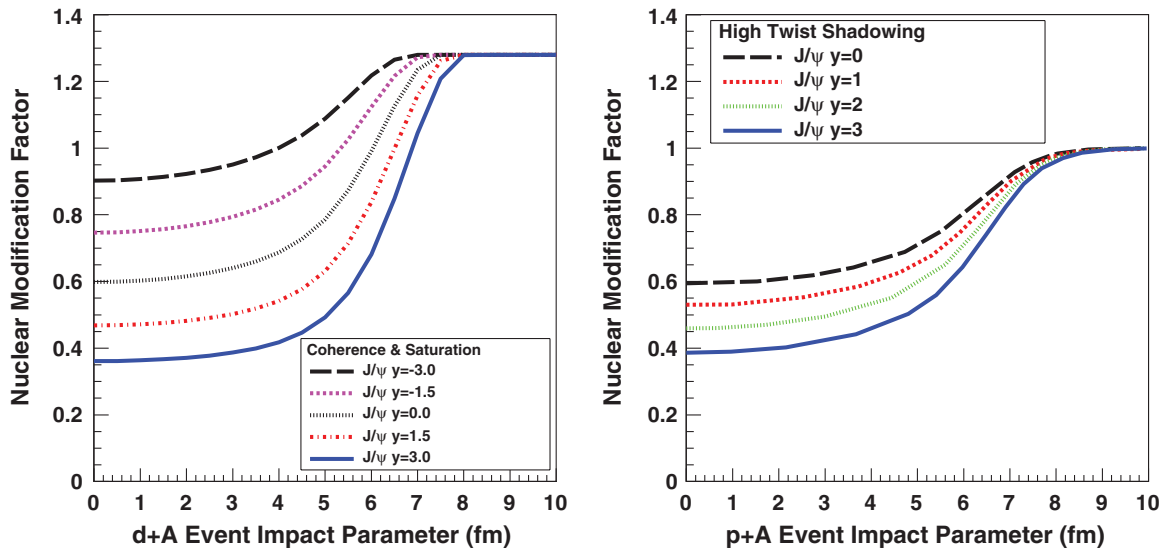


FIG. 15. (Color online) Left panel: The J/ψ nuclear-modification results from the color-glass condensate calculation, including gluon saturation, from Ref. [31], as a function of event impact parameter in $d + Au$ reactions. Right panel: The results of a coherence and color-transparency calculation [33] for the J/ψ nuclear modification as a function of event impact parameter in $p + Au$ reactions.

EPS09 parameter set 5, $\sigma_{br} = 4$ mb, and the initial-state energy loss corresponds to approximately $\Delta E/E \approx 0.005/\text{fm}^2 \times L^2$. Again, although the R_{CP} fit is reasonable, there is no global agreement for the R_{dAu} data.

These results are a first attempt at comparing the simplest initial-state energy-loss calculation to the recent J/ψ data. We have not included Poisson fluctuations of the radiated quanta, which are important when one is near the very-high- x_1 limit, as pointed out in Ref. [28]. However, in their calculation, they have not included fluctuations in the L value itself, as we have done through utilizing N_{tube} [before].

VI. ADDITIONAL MODEL COMPARISONS

Our calculation results presented thus far include no explicit coherence effects (either initial or final state). In this section, we discuss two such published calculations and check if they are able to reproduce the experimental data.

One such proposal incorporates the saturation of strong gluon fields in the incoming nucleus (nonlinear evolution of the gluon distributions at low x). In the PHENIX paper [1], the data were compared with a color-glass condensate calculation [30] that incorporated suppression at low x from gluon saturation and enhancement from double-gluon exchange diagrams. Recent calculations following this framework [31] include a more accurate treatment of the nuclear geometry and the dipole-nucleus scattering amplitudes, and are calculated in a consistent fashion with recent results for nucleus-nucleus collisions [32]. Figure 15 (left panel) shows the calculated J/ψ nuclear modification for different rapidities as a function of the $d + Au$ event impact parameter (b). It is notable that for large b , there is a 30% nuclear enhancement, even though the coherence is only in the longitudinal direction and the local nuclear density for these large- b events is small.

In a second coherence calculation, as presented in Ref. [33], the J/ψ production is determined by coherence and color-transparency effects. Figure 15 (right panel) shows the calculated J/ψ nuclear-modification factor as a function of event impact parameter in $p + Au$ reactions.

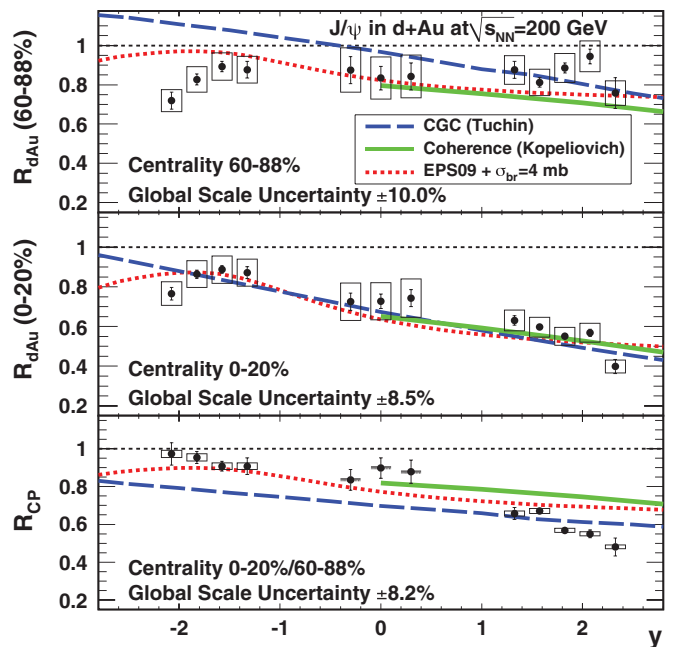


FIG. 16. (Color online) The PHENIX experimental data for J/ψ R_{dAu} peripheral (top), R_{dAu} central (middle), and R_{CP} 0-20%/60-88% (bottom), as a function of rapidity. The solid (green) curve results from Ref. [33] with coherence effects and color transparency. The dashed (blue) curve is the color-glass condensate calculation [31]. The dotted (red) curve is our calculation with nPDF EPS09 default set = 1, with a linear geometric dependence and $\sigma_{br} = 4$ mb.

In either case, we can fold these dependencies with the $d + \text{Au}$ event impact parameter distributions or the r_T distribution (for the $p + \text{Au}$ predictions), and compute the $R_{d\text{Au}}$ and R_{CP} modification factors, as shown in Fig. 16. We show for comparison the EPS09 nPDF default with linear geometric dependence and $\sigma_{br} = 4$ mb. The calculation from Ref. [33] yields similar results to the EPS09 nPDF and σ_{br} calculation, and has insufficient suppression at the most forward rapidity. The color-glass condensate calculation shows better agreement at forward rapidity, though the rapidity dependence is not as steep as that of the R_{CP} experimental data. However, there is substantial disagreement with the data at mid and backward rapidities. Note that that calculation assumes coherence over the entire longitudinal extent of the nucleus, but this coherence approximation is no longer valid at some higher- x_2 values (i.e., at mid and backward rapidity). It is also no longer valid for low densities that occur at large impact parameter values. Thus the enhanced $R_{d\text{Au}}$ calculated in peripheral collisions (shown in the left panel of Fig. 15) is likely to be in a region outside the range of validity of the calculation.

VII. SUMMARY

In this paper, we have presented calculations for J/ψ nuclear modifications including effects of modified parton distribution functions (nPDFs) and fit parameter σ_{br} . Utilizing the full set of EPS09 nPDFs and three different postulated geometric dependencies, we found that the calculations cannot be reconciled with the full rapidity and centrality dependence of the PHENIX $d + \text{Au}$ J/ψ data. Additionally, comparison of the calculations with plots of R_{CP} versus $R_{d\text{Au}}$ indicate that

even a much larger σ_{br} at forward rapidity cannot reconcile the calculation with the data, since the σ_{br} contribution always has an exponential geometric dependence, which is inconsistent with the trend required by the data. Incorporation of initial-state parton energy loss yields an improved description of the $J/\psi R_{\text{CP}}$, but without a good simultaneous description of $R_{d\text{Au}}$. Additional constraints from Drell-Yan and direct photon observables at forward rapidity and at different $\sqrt{s_{NN}}$ energies may be necessary to help constrain contributions from energy loss. We also compared two different coherence calculations to the data and find no agreement across all rapidities and centralities. Thus, a fully quantitative understanding of J/ψ modifications remains elusive.

ACKNOWLEDGMENTS

We thank Kirill Tuchin for providing us with the color-glass condensate calculation results and useful discussions, and Michael Stone for generating the PYTHIA event samples. We also acknowledge useful discussions with Mike Leitch, Darren McGlinchy, and Ramona Vogt. J.L.N and M.G.W acknowledge funding from the Division of Nuclear Physics of the US Department of Energy under Grant No. DE-FG02-00ER41152. L.A.L.L acknowledges that this work was performed under the auspices of the US Department of Energy by Lawrence Livermore National Laboratory under Contract No. DE-AC52-07NA27344. A.D.F acknowledges funding from the National Science Foundation under Contract No. PHY-07-56474. We also thank the Institute for Nuclear Theory at the University of Washington for its hospitality and the US Department of Energy for partial support during some of this work.

-
- [1] A. Adare *et al.*, *Phys. Rev. Lett.* **107**, 142301 (2011).
 - [2] C. Lourenco, R. Vogt, and H. K. Woehri, *JHEP* **02** (2009) 014.
 - [3] A. Adare *et al.* (PHENIX Collaboration), *Phys. Rev. C* **77**, 024912 (2008).
 - [4] R. Vogt, *Phys. Rev. C* **71**, 054902 (2005).
 - [5] D. Kharzeev, C. Lourenco, M. Nardi, and H. Satz, *Z. Phys. C* **74**, 307 (1997).
 - [6] K. J. Eskola, H. Paukkunen, and C. A. Salgado, *JHEP* **04** (2009) 065.
 - [7] S. J. Brodsky and J.-P. Lansberg, *Phys. Rev. D* **81**, 051502 (2010).
 - [8] J. P. Lansberg, *Eur. Phys. J. C* **61**, 693 (2009).
 - [9] C. Lourenco, P. Faccioli, and H. K. Wohri, *Lect. Notes Phys.* **785**, 199 (2010).
 - [10] M. L. Miller, K. Reygers, S. J. Sanders, and P. Steinberg, *Annu. Rev. Nucl. Part. Sci.* **57**, 205 (2007).
 - [11] S. R. Klein and R. Vogt, *Phys. Rev. Lett.* **91**, 142301 (2003).
 - [12] B. Alver and G. Roland, *Phys. Rev. C* **81**, 054905 (2010).
 - [13] P. Sorensen, *J. Phys. G* **37**, 094011 (2010).
 - [14] J. L. Nagle, P. Steinberg, and W. A. Zajc, *Phys. Rev. C* **81**, 024901 (2010).
 - [15] H.-J. Drescher, A. Dumitru, C. Gombeaud, and J.-Y. Ollitrault, *Phys. Rev. C* **76**, 024905 (2007).
 - [16] PHOBOS Collaboration, B. Alver *et al.*, *Phys. Rev. Lett.* **98**, 242302 (2007).
 - [17] K. Nakamura and Particle Data Group, *J. Phys. G* **37**, 075021 (2010).
 - [18] A. Rakotozafindrabe, E. G. Ferreira, F. Fleuret, and J. P. Lansberg, *J. Phys. G* **37**, 094055 (2010).
 - [19] E. G. Ferreira, F. Fleuret, J. P. Lansberg, and A. Rakotozafindrabe, *Phys. Rev. C* **81**, 064911 (2010).
 - [20] E. Ferreira, F. Fleuret, J. Lansberg, and A. Rakotozafindrabe, *Phys. Lett. B* **680**, 50 (2009).
 - [21] T. Sjostrand, S. Mrenna, and P. Skands, *JHEP* **05** (2006) 026.
 - [22] J. Nagle and M. Bennett, *Phys. Lett. B* **465**, 21 (1999).
 - [23] D. Kharzeev, M. Nardi, and H. Satz, *Phys. Lett. B* **405**, 14 (1997).
 - [24] PHENIX Collaboration, A. Adare *et al.*, *Phys. Rev. C* **77**, 064907 (2008).
 - [25] N. Brambilla *et al.*, *Eur. Phys. J. C* **71**, 1534 (2011).
 - [26] J. Moss *et al.*, *arXiv:hep-ex/0109014*.
 - [27] M. B. Johnson *et al.*, *Phys. Rev. C* **65**, 025203 (2002).
 - [28] R. Neufeld, I. Vitev, and B. Zhang, *arXiv:1010.3708*.
 - [29] P. E. Reimer, *J. Phys. G* **34**, S107 (2007).
 - [30] D. Kharzeev and K. Tuchin, *Nucl. Phys. A* **770**, 40 (2006).
 - [31] K. Tuchin (private communication).
 - [32] K. Tuchin, *Nucl. Phys. A* **830**, 243c (2009).
 - [33] B. Z. Kopeliovich, I. K. Potashnikova, H. J. Pirner, and I. Schmidt, *Phys. Rev. C* **83**, 014912 (2011).